Light-Induced Reorientation Transition in an Antiferromagnetic Semiconductor

Bryan T. Fichera,[1,*,**] Baiqing Lv,[1,2,*] Karna Morey,[1,†] Zongqi Shen,[1] Changmin Lee,[3,4] Elizabeth Donoway,[5] Alex Liebman-Peláez,[5] Anshul Kogar,[1,‡] Takashi Kurumaji,[1,§] Martin Rodriguez-Vega,[6,7] Rodrigo Humberto Aguilera del Toro,[8,9] Mikel Arruabarrena,[9] Batyr Ilyas,[1] Tianchuang Luo,[1] Peter Müller,[10] Aritz Leonardo,[8,11] Andres Ayuela,[8,9] Gregory A. Fiete,[1,6] Joseph G. Checkelsky,[1] Joseph Orenstein,[3,5] and Nuh Gedik[1,‖]

[1]*Department of Physics, Massachusetts Institute of Technology, Cambridge, Massachusetts 02139, USA*
[2]*Tsung-Dao Lee Institute, School of Physics and Astronomy, and Zhangjiang Institute for Advanced Study, Shanghai Jiao Tong University, Shanghai, 200240, China*
[3]*Materials Science Division, Lawrence Berkeley National Laboratory, Berkeley, California 94720, USA*
[4]*Department of Physics, Hanyang University, Seoul 04763, Republic of Korea*
[5]*Department of Physics, University of California at Berkeley, Berkeley, California, USA*
[6]*Department of Physics, Northeastern University, Boston, Massachusetts 02115, USA*
[7]*Department of Physics, The University of Texas at Austin, Austin, Texas 78712, USA*
[8]*Donostia International Physics Center (DIPC), 20018 Donostia-San Sebastián, Spain*
[9]*Centro de Física de Materiales-Materials Physics Center (CFM-MPC), 20018 Donostia-San Sebastián, Spain*
[10]*X-Ray Diffraction Facility, Department of Chemistry, Massachusetts Institute of Technology, Cambridge, Massachusetts 02139, USA*
[11]*EHU Quantum Center, University of the Basque Country UPV/EHU, 48940 Leioa, Spain*

(Received 13 March 2024; revised 29 October 2024; accepted 20 December 2024; published 26 February 2025)

Because of the lack of a net magnetic moment, antiferromagnets possess a unique robustness to external magnetic fields and are thus predicted to play an important role in future magnetic technologies. However, this robustness also makes them quite difficult to control, and the development of novel methods to manipulate these systems with external stimuli is a fundamental goal of antiferromagnetic spintronics. In this work, we report evidence for a metastable reorientation of the order parameter in an antiferromagnetic semiconductor triggered by an ultrafast quench of the equilibrium order via photoexcitation above the band gap. The metastable state forms less than 10 ps after the excitation pulse, and persists for longer than 150 ps before decaying to the ground state via thermal fluctuations. Importantly, this transition cannot be induced thermodynamically, and requires the system to be driven out of equilibrium. Broadly speaking, this phenomenology is ultimately the result of large magnetoelastic coupling in combination with a relatively low symmetry of the magnetic ground state. Since neither of these properties are particularly uncommon in magnetic materials, the observations presented here imply a generic path toward novel device technology enabled by ultrafast dynamics in antiferromagnets.

DOI: 10.1103/PhysRevX.15.011044

Subject Areas: Condensed Matter Physics, Strongly Correlated Materials

I. INTRODUCTION

When the Hamiltonian of a system contains multiple interaction strengths of comparable magnitude, the corresponding free energy is often host to a diverse collection of metastable states just barely separated in energy from the true ground state. This phenomenology results in an extreme sensitivity to external stimuli [1–3], which can be exploited in an ultrafast way using light to drive transitions between these states [4–7].

One important application is in magnetic devices, where the electron spins form an ordered state in equilibrium and may thus be used to store information. Antiferromagnets (AFMs) have received special attention in this regard, as

*These authors contributed equally to this work.
†Present address: Department of Physics, Stanford University, Stanford, California, 94305, USA.
‡Present address: Department of Physics and Astronomy, University of California, Los Angeles, California, USA.
§Present address: California Institute of Technology, 1200 E California Blvd., Pasadena, California 91125, USA.
‖Contact author: gedik@mit.edu
**Present address: Materials Science Division, Argonne National Laboratory, Lemont, Illinois 60439, USA.

they possess zero net magnetic moment and are thus robust to stray magnetic fields from adjacent magnetic devices [8]. The dominance of exchange rather than anisotropy energies in the dynamics of spins which are antiferromagnetically ordered also leads to order-of-magnitude faster switching timescales compared to their ferromagnetic counterparts [9].

Importantly, the ground state of an AFM is typically not unique, with the number of degenerate states (corresponding generically to various rotations of the AFM order parameter) being determined by the number of symmetries which are broken at the magnetic ordering temperature. In the context described above, this degeneracy invites the possibility of an ultrafast antiferromagnetic device which uses light to switch between these different states. Moreover, if the symmetry of the magnetic phase is sufficiently low (relative to the parent phase), the number of such states can be quite high, and a multistep magnetic memory might be constructed which operates via ultrafast reorientation transitions of the AFM order parameter between states that are not antiparallel.

Broadly speaking, one can distinguish two different approaches for achieving such transitions in real materials. In the first case, one imagines manipulating the AFM orientation "coherently" by, for example, resonantly driving an infrared-active phonon mode to large amplitude, although this usually requires large electric fields (as the relevant light-matter interactions are usually highly nonlinear [10]) which are difficult to obtain in the frequency range associated with phonons in crystals. An alternative mechanism—which has been shown to occur abundantly in superconductivity (SC) [7] and charge density wave (CDW) [5] systems—is to *quench* the equilibrium order by exciting carriers above the band gap, and then exploit the subsequent relaxation dynamics which may, in the right system, show a preference for one state over the other [11]. In contrast to the case of resonant phonon driving, this mechanism involves primarily electronic excitations and therefore requires relatively little energy if the photon frequency is above the band gap. However, despite successful demonstrations of this approach in nonmagnetic systems [5,7], evidence for this mechanism occurring in AFMs does not currently exist, and whether the phenomenology described here actually occurs in real magnetic materials remains a fundamental open question.

In this work, we report a light-induced phase transition between nearly degenerate AFM states in the antiferromagnetic semiconductor $CaMn_2Bi_2$ [12] triggered by an ultrafast quench of the equilibrium order parameter with a femtosecond light pulse. Using time-resolved second harmonic generation (TRSHG), a pump-probe technique sensitive to the magnitude and direction of the AFM order parameter, we find that above-gap optical excitation indeed causes the system to reorient to a new, metastable orientation of the AFM order parameter. The transition is fast (occurring less than 10 ps after photoexcitation), requires low pump fluence ($\sim$200 $\mu J\,cm^{-2}$ vs $\sim$10 $mJ\,cm^{-2}$ [10]), and cannot be induced thermodynamically. These findings suggest that the same postquench, metastable dynamics occurring in nonmagnetic systems [5,7] applies to AFMs as well, opening the door to potential optospintronic device architectures exploiting nonequilibrium phase transitions between different nearly degenerate states.

II. RESULTS

A. Equilibrium

Crystallographically, $CaMn_2Bi_2$ consists of a puckered-honeycomb tiling of Mn atoms with a high-temperature crystallographic point group of $\bar{3}m$ [see Fig. 1(a)]. The electronic gap is on the order of 4 meV [see Fig. 1(b) and Supplemental Material, Fig. S18(a) [13]] and is thought to be due to a delicate combination of correlations and hybridization between relatively localized Mn $3d$ states and dispersive Bi $6p$/Mn $4s$ hybrid bands [12,23–25]. Néel-type antiferromagnetic long-range order with spins lying in the ab plane develops in this material at $T_c \sim 150$ K, accompanied by a kink in the electrical resistivity [Fig. 1(b)] and magnetization [Supplemental Material, Fig. S18(b)] and the appearance of a new peak in the

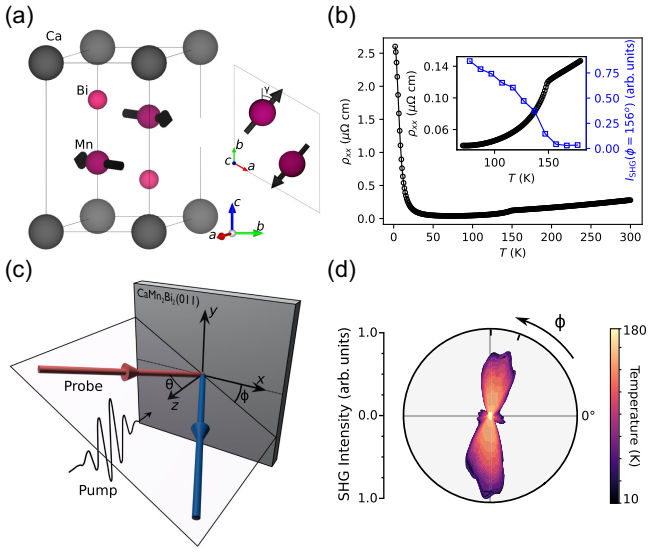

FIG. 1. (a) Magnetic unit cell of $CaMn_2Bi_2$. The angle γ is such that the Mn spin does not lie precisely along any particular crystallographic axis. (b) Resistivity as a function of temperature for a representative sample. The inset shows an enlarged view of the resistivity near T_c plotted against the SHG intensity integrated across the region indicated in (d). (c) Schematic of the rotational-anisotropy SHG (RASHG) setup. The crystallographic a axis lies along the dashed line (see Supplemental Material, Sec. S5 [13]). (d) Temperature dependence of the RASHG intensity in the P_{in}–P_{out} polarization channel from the (011) surface of $CaMn_2Bi_2$. Other polarization channels are shown in the Supplemental Material, Fig. S2. The area between the two ticks indicates the region integrated to produce the inset of (b).

powder neutron diffraction [12]. Importantly, the powder neutron refinement indicates that the ordered moments are slightly misaligned with the a and b axes of the high-symmetry phase [see Fig. 1(a)], so that the low-temperature magnetic point group is $\bar{1}'$; i.e., the only symmetries that are preserved in the low-temperature phase are the identity operator and the product of inversion and time reversal [12]. The remarkably low symmetry of this magnetic ground state is likely due to highly frustrated magnetic interactions, as suggested by the proximity of isostructural $CaMn_2Sb_2$ to a mean-field magnetic tricritical point [26,27]. In contrast, the lattice is thought to remain fully symmetric at all temperatures, so that the symmetry breaking at T_c is solely due to the AFM order [this is verified with single-crystal x-ray diffraction (XRD); see Supplemental Material, Fig. S8 [13]].

As spin-orbit coupling is expected to be strong in this material, the breaking of inversion symmetry by the magnetic order should result in a strong second harmonic generation (SHG) signal below T_c, despite the fact that the lattice remains centrosymmetric [28,29]. We probe this SHG signal using a rotational-anisotropy SHG (RASHG) apparatus [Fig. 1(c)] which measures the reflected second harmonic intensity as the plane of incidence (and the incoming and outgoing polarization vectors, which may be P or S polarized relative to the plane of incidence) is rotated about the sample normal [30–32]. Figures 1(b) and 1(d) depict the SHG signal from the (011) surface of $CaMn_2Bi_2$ as a function of temperature across T_c, demonstrating that RASHG is indeed sensitive to the magnetic order in this material.

Frequently, AFM materials may host intricate domain configurations, the details of which greatly impact the relevant magnetic functionalities [33,34]. Because the low-temperature magnetic point group of $CaMn_2Bi_2$ breaks multiple symmetries of the high-temperature point group, we indeed expect that the low-temperature magnetic ground state should involve some number of energetically degenerate domains. In Fig. 2, we characterize these domains using a combination of RASHG and a spatially resolved optical polarimetry technique known as photothermal modulated birefringence (PTMB), which is a sensitive technique for measuring small changes in the anisotropic index of refraction (and consequently, the direction of the AFM order parameter) [35,36].

Figure 2(a) shows the PTMB signal from the (011) surface of $CaMn_2Bi_2$ above T_c (see Supplemental Material, Sec. S7 and Fig. S22 [13]). No contrast is found within a $\sim 500 \times 500\ \mu m^2$ area on the sample, demonstrating that the thermally modulated index of refraction is spatially uniform at high temperature. As the temperature is lowered below T_c [Fig. 2(c)], a pronounced contrast appears in the PTMB map which indicates the presence of two separate AFM domains with different order parameter directions.

While PTMB is nominally sensitive to the direction of the AFM order parameter, it cannot differentiate between 180° domains as it couples only to the linear index of refraction of the material. Therefore, it is not clear from PTMB alone whether the domains in Fig. 2(c) are truly homogeneous or may contain a mixture of 180° domains. In contrast, nonlinear spectroscopies like SHG can differentiate 180° AFM domains due to an interference between the SHG sources (e.g., electric dipole, magnetic dipole, and electric quadrupole; see Supplemental Material, Fig. S20 [13]) which transform differently under time-reversal symmetry [37–40]. This effect can be especially pronounced in the presence of magnetostriction [39]. We thus proceed to investigate the presence of 180° domains in this material using RASHG.

Figures 2(d)–2(g) depict the RASHG results at 8 K in the two regions identified in Fig. 2(c). The same crystal piece was used for both measurements. As with PTMB, we do find that the SHG domains are large and apparently homogeneous (on a scale of hundreds of microns; see Supplemental Material, Fig. S16 [13]). Surprisingly, however, in different cooldowns we observe that the RASHG pattern in the leftmost region of Fig. 2(c) randomly takes the form of either Fig. 2(d) or Fig. 2(e), and in the rightmost region, it takes the form of either Fig. 2(f) or Fig. 2(g). In contrast, the PTMB does not change upon thermal cycling (see Supplemental Material, Fig. S21).

Since the four domains in Figs. 2(d)–2(g) have different RASHG patterns, they correspond to four different AFM domains with different values of the Néel vector [defined as the difference in the magnetic moment on the two Mn sublattices; see Fig. 1(a)]. While the RASHG refinement (see Supplemental Material, Sec. S3 [13]) does not explicitly determine the value of the Néel vector in each of these domains, the fact that the RASHG pattern changes on thermal cycling while the PTMB signal does not indicates that each pair of domains in Fig. 2 consists of two domains with 180°-opposite Néel vectors. Furthermore, there is a relative angle between Figs. 2(d) and 2(e) and Figs. 2(f) and 2(g), since they have different PTMB signals [41]. An example of a domain assignment satisfying these criteria is depicted schematically in the insets of Figs. 2(d)–2(g), where the AFM order parameter is represented by two red arrows. Importantly, within a single location, the two opposite orientations are accessible via thermal cycling; hence, they are energetically degenerate. We have verified that the relationship between domains described here is consistent with the SHG susceptibility tensors [42] extracted by fitting the data in Fig. 2 (see Supplemental Material, Sec. S3). In addition, our data are not consistent with an alternative interpretation involving the interference of two independent order parameters (see Supplemental Material, Sec. S2 [13]).

B. Nonequilibrium

Having demonstrated that $CaMn_2Bi_2$ hosts an elaborate free-energy surface with multiple degenerate or nearly

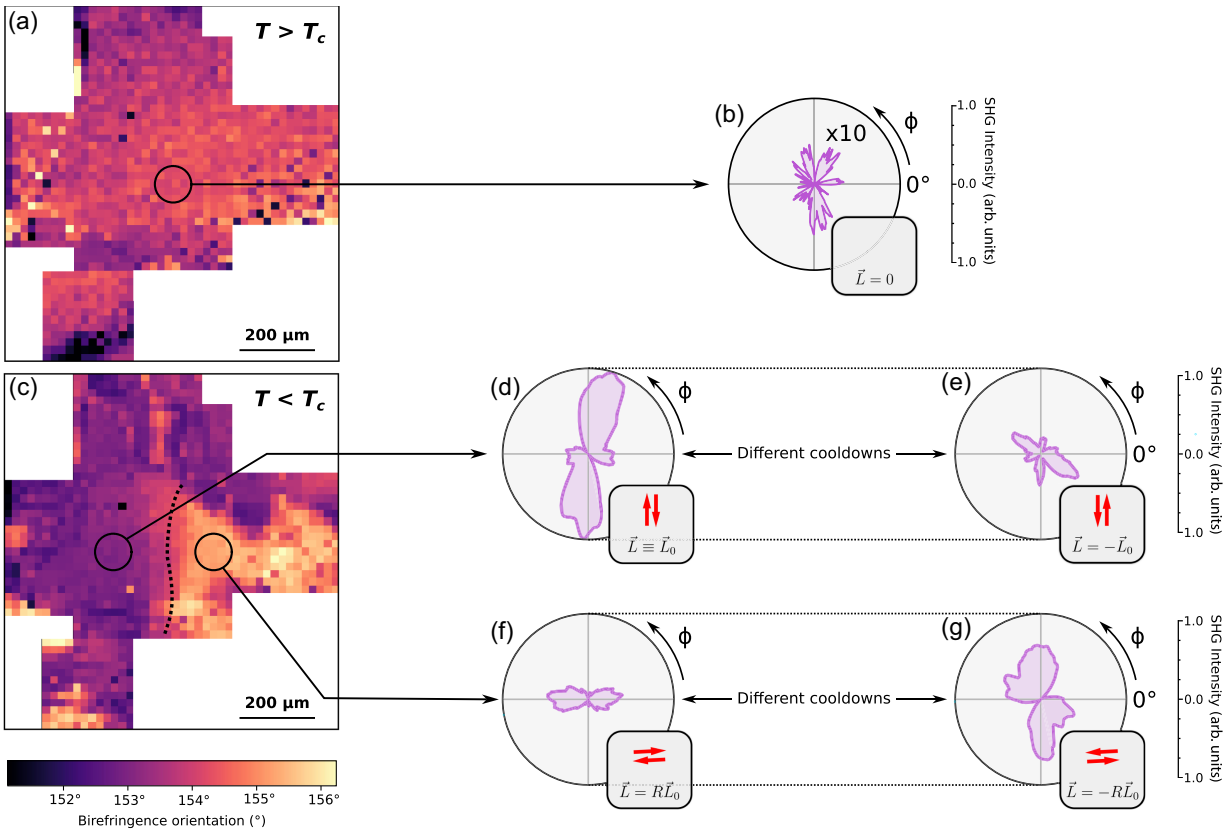

FIG. 2. (a) Birefringence orientation map for $T = 200$ K $> T_c$. (b) RASHG intensity in the P_{in}–P_{out} polarization channel for the region indicated in (a) at 157 K. Other polarization channels are shown in the Supplemental Material, Fig. S10 [13]. (c) Birefringence orientation map for $T = 152.5$ K $< T_c$. (d),(e) RASHG intensity at 8 K in the P_{in}–P_{out} polarization channel for consecutive cooldowns for the region indicated in (c). The system randomly chooses the RASHG pattern in (d) or (e) on each cooldown. (f),(g) RASHG intensity at 8 K in the P_{in}–P_{out} polarization channel for consecutive cooldowns for the region indicated in (c). The system randomly chooses the RASHG pattern in (f) or (g) on each cooldown. Other polarization channels are shown in the in the Supplemental Material, Fig. S10. The insets beneath the RASHG plots depict the relationships between the Néel vectors $\vec{L}$ associated with each domain, as determined from the RASHG and PTMB data: RASHG patterns on the same spot but different cooldowns correspond to Néel vectors which are related by an overall sign ($\vec{L} = \pm\vec{L}_0$ and $\vec{L} = \pm R\vec{L}_0$), whereas those on different spots are related by an element R (not identity or inversion) of the high-symmetry point group D_{3d}. Neither the value of $\vec{L}_0$ nor the operation R are explicitly determined by these measurements. Note that the RASHG experiments are performed normal to the (011) plane (see Fig. 1), whereas the vectors in the insets are drawn in the (001) plane.

degenerate ground states, we now turn to the question of whether light can be used to manipulate or possibly switch between these states. To answer this question, we pump each of the order parameter directions identified in Fig. 2 at 8 K with a ∼100-fs normally incident near-infrared light pulse ($\hbar\omega \approx 1$ eV) and probe the AFM order parameter with RASHG using a subsequent probe pulse. By varying the delay Δt between the two pulses, we create a series of snapshots of the AFM order parameter at different times following excitation. The results are shown in Fig. 3, where the four rows correspond to the four order parameter directions identified in Fig. 2, and the horizontal axis is the time delay between the pump and probe pulses. The first two rows [Figs. 3(a) and 3(b)] correspond to the leftmost domain in Fig. 2(c), for which it is found that, after pumping, the strength of the RASHG signal is quickly extinguished. After a delay of around ∼8–10 ps, the AFM order recovers so that the shape of the RASHG pattern is similar to before zero delay up to small changes in the relative peak heights. The order parameter magnitude and direction inferred by this data are depicted schematically in the insets of Figs. 3(a) and 3(b).

The striking observation is in the bottom two rows [Figs. 3(c) and 3(d)], which depict the time-resolved RASHG results in the rightmost domain of Fig. 2(c). In this domain, the RASHG signal again quickly decreases, and the shape does not initially change. However, roughly ∼6–8 ps after excitation, the RASHG pattern abruptly changes shape, so that the pattern after ∼10 ps is equivalent to Fig. 3(a). Together with the findings of Fig. 2, these results suggest that the final state in Figs. 3(c) and 3(d) is one in which the AFM order parameter direction has indeed

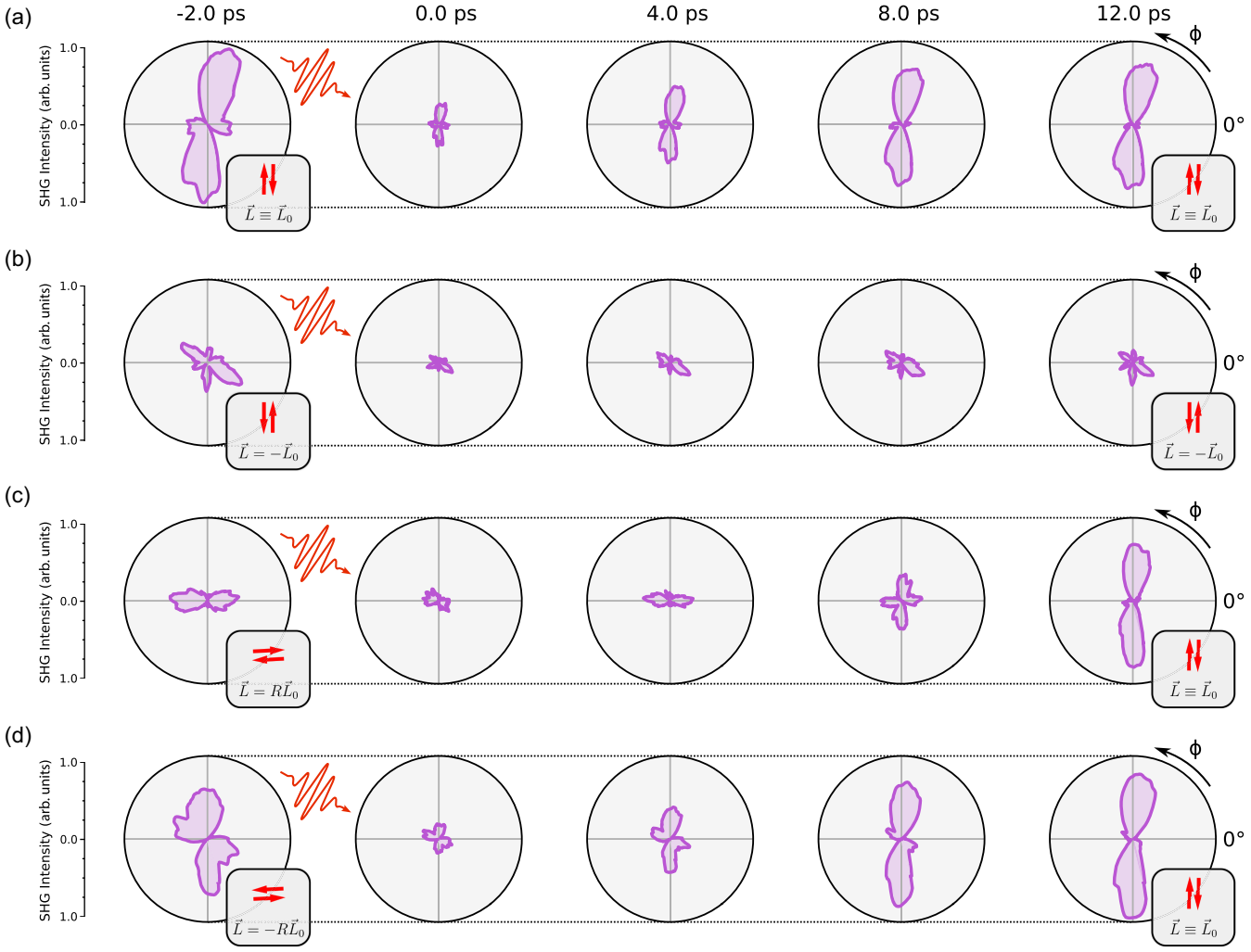

FIG. 3. RASHG intensity at 8 K in the P_{in}–P_{out} polarization channel as a function of time for the AFM order parameter identified in (a) Fig. 2(d), Fig. 2(e), Fig. 2(f), and Fig. 2(g). Other polarization channels are shown in the Supplemental Material, Fig. S11 [13]. The pump fluence is set to ∼600 μJ cm^{-2}. The insets beneath the RASHG plots depict schematically the value of the Néel vector 2 ps before and 12 ps after photoexcitation, as in Fig. 2.

been reoriented relative to equilibrium. Remarkably, one must use light to reach this metastable state as it is not present in thermal equilibrium at this spot.

We performed the above measurements out to $\Delta t \gtrsim$ 150 ps (see Supplemental Material, Fig. S14 [13]) and found that the reoriented state persists at least this long before relaxing back to equilibrium in time for the next pair of pulses to arrive (roughly 200 μs later). As the pump fluence is decreased (see Supplemental Material, Fig. S5), the effect of the excitation is diminished until, at low fluences (∼100 μJ cm^{-2}), the final state is equivalent to the initial state, and only small changes to the SHG (associated with dynamics that do not launch the system into the metastable state) are visible near zero delay. Interestingly, which of the two opposite directions [Fig. 2(d) or Fig. 2(e)] the magnetic order favors after excitation is consistent from pulse to pulse, but not from one sample to another (see Supplemental Material, Figs. S13 and S14), suggesting that, below the magnetic ordering temperature, interactions between neighboring domains break the degeneracy between these states. Finally, we note that no aspect of these observations changes with the polarization of the pump pulse (see Supplemental Material, Fig. S12 [13]).

III. DISCUSSION

Taken together, these considerations indeed point to a bona fide ultrafast phase transition in $CaMn_2Bi_2$ induced by a femtosecond light pulse. We now seek to understand, at least qualitatively, the microscopic nature of this transition. Before discussing the time-resolved data of Fig. 3, we must first understand the equilibrium phenomenology implied by Fig. 2. Group theory (see Supplemental Material, Sec. S1.3 [13]) suggests that there should be 12 energetically degenerate order parameter directions (see Supplemental Material, Fig. S17), independent of location

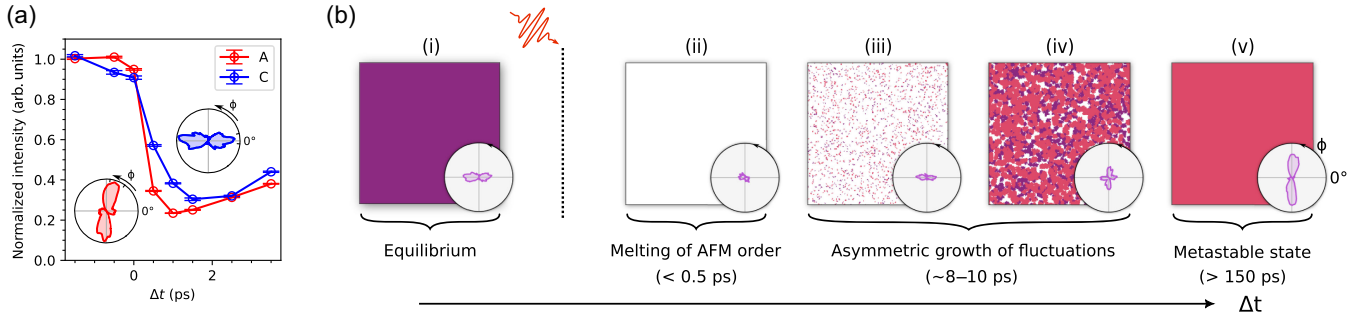

FIG. 4. (a) Integrated SHG intensity as a function of time corresponding to Fig. 3(a) (A, red) and Fig. 3(c) (C, blue). Error bars were calculated as described in Supplemental Material, Sec. S4 [13]. Insets show the equilibrium SHG patterns in the P_{in}–P_{out} polarization combination for the two domains, with the integration region indicated. The y-axis normalization for either domain is defined such that the average signal before zero delay is equal to 1.0. (b) Conceptual illustration of the dynamics following laser excitation as described in the text. Ultrafast melting of the AFM order (i) and (ii) is followed by the rapid growth of fluctuations (iii) and (iv), with the final state (v) determined by the relative growth rate of different orders. Insets show the RASHG data of Fig. 3(c) corresponding roughly to each of these steps. The fluctuation growth step (iii) and (iv) may occur with or without a background of coherent oscillations (see Supplemental Material, Secs. S1.2 and S1.3 [13]).

on the sample. However, only two directions are observed per measurement location in our experiment. This observation is explained by recognizing that local strain fields in the material are expected to pole the long-range order (see Supplemental Material, Sec. S1.1), so that certain order parameter directions are energetically favored relative to others at a given spot [43–46]. Since these strain fields may vary from one location to another (the details of which depend subtly on the local growth conditions), different locations on the sample would then show different sets of RASHG patterns, in agreement with the findings of Fig. 2. This picture also explains the observation that opposite AFM configurations are energetically degenerate, as strain itself is inherently symmetric under 180° rotations.

Turning now to the nonequilibrium phenomenology (Figs. 3 and 4), we begin by noting that the sudden suppression of the SHG intensity at early times indicates that the primary effect of the pump pulse is simply to quench the AFM order parameter [Figs. 4(b) and 4(c)]. According to recent theoretical work based on the time-dependent Ginzburg-Landau (TDGL) equation [11,47], the dynamics following such a quench are governed not by the global minimum of the free energy, but rather by the exponential amplification of spatial order parameter fluctuations [Figs. 4(d) and 4(e)], which may occur differently for different orders (Supplemental Material, Sec. S1.2 [13]). The final state of the transition [Fig. 4(f)] is then determined by which state supports the fastest-growing fluctuations. In the context of light-induced SC [7,48], for example, the dominant order in equilibrium is a CDW, whose fluctuations naturally involve motion of the massive nuclei and are thus much slower than fluctuations of the SC order parameter [11,49]. Note that, in the general case, the final state is determined not just by the relaxation rates, but also by their start times; that is, if one order is *quenched* faster than another, fluctuations of that order are afforded a longer period to grow and may thus dominate at long times.

In our system, the relatively slow (~8–10 ps; see Fig. 3) recovery timescale indicates that the dynamics of the AFM order parameter, like the CDW order of Ref. [7], also likely involve motion of the atomic nuclei (i.e., magnetoelastic coupling). However, in contrast to the CDW-SC competition referred to above, the dominant and subdominant orders in our system correspond not to completely different orders, but rather to different orientations of the same order. One would thus naively expect the corresponding fluctuations to exhibit more or less the same dynamics. However, as described above, this naive symmetry of the material is in fact broken at all temperatures by the internal strain; it is therefore appropriate to think of the two nonparallel AFM orientations as truly distinct orders, and the TDGL analysis described above thus applies rigorously to $CaMn_2Bi_2$. The situation is similar to the case of $LaTe_3$, where the equilibrium and nonequilibrium orders are both CDWs which are split by a small lattice anisotropy [5]. Importantly, it is noted in Ref. [11] that small variations in the density of different fluctuations are exponentially amplified as the system relaxes, so that only a modest difference in the relevant dynamics is sufficient to favor the metastable state as the system recovers. Such asymmetric amplification of nonparallel AFM orientations thus likely forms the basis for the reorientation transition in $CaMn_2Bi_2$.

Additional evidence supporting this general picture may be found by examining the time dependence of the SHG signal at short times [Fig. 4(a)], before the order parameter switches to the metastable state. In particular, on examining the initial decay rates it can be seen that the SHG signal corresponding to Fig. 3(a) reaches 30% of its original value just 0.5 ps after zero delay; the equivalent drop in SHG intensity for Fig. 3(c) takes > 0.5 ps longer. That is, the

time required to quench the final state is approximately half the time needed to quench the initial state. As a result, long-wavelength fluctuations of the subdominant, metastable order experience a longer period of exponential amplification compared to the equilibrium order, which may explain the dominance of the metastable state at long times (see Ref. [11], Sec. V). The metastability of the final state is provided by the fact that the long-term relaxation dynamics are presumably dependent on the thermal nucleation and subsequent motion of AFM domain walls, which can be quite slow [50,51]. Finally, we remark that while the quench dynamics described here can explain all features of our data, they also likely occur alongside a background of coherent excitations (e.g., coherent phonons, which are observable in time-resolved reflectivity; see Supplemental Material, Fig. S6 [13]) which can couple to the order parameter via the lattice strain (see Supplemental Material, Sec. S1.3). While no evidence of these excitations is apparent in our SHG data, further studies will be needed to determine the extent to which they might still be important.

IV. CONCLUSION

To summarize, we have presented evidence of a magnetic reorientation transition in the antiferromagnetic semiconductor $CaMn_2Bi_2$ induced by above-gap optical excitation. Looking forward, we note two ingredients that seem to be most important for the transition demonstrated in this work: low symmetry, so that there are multiple energetic minima in the magnetic phase, and, presumably, some degree of magnetoelastic coupling, so that the different minima are not precisely degenerate in thermal equilibrium. Neither of these properties are unique to $CaMn_2Bi_2$, and analogous materials may exist with similar light-induced phenomenology. The apparently pronounced coupling between light and magnetic order in this material also invites the fascinating possibility that related phenomenology could also be accessed via additional tuning parameters like strain or current. This is a key prediction of so-called $\mathcal{PT}$-symmetric systems, in which inversion and time-reversal symmetries are independently broken but the product of the two is preserved [52–54]. Further investigation of these and related compounds could have far-reaching impacts for future optospintronic technology.

V. METHODS

A. Material growth

Single crystals of $CaMn_2Bi_2$ were grown by a Bi flux method following Ref. [12]. The starting materials were Ca ingot, Mn powder, and Bi powder. They were loaded into an alumina crucible in the molar ratio of $Ca:Mn:Bi = 1:2:10$, which was sealed in an evacuated quartz tube. The ampoule was heated to 1000 °C and kept at this temperature for 11 hours before being slowly cooled to 400 °C in 10 days. The excess flux was removed by a centrifuge at this temperature. The single phase nature of the crystals was checked by powder XRD and the orientation was checked by a single-crystal x-ray diffractometer.

B. TRSHG measurements

The TRSHG measurements were performed using a fast-rotating optical grating method—where the plane of incidence is rotated about the normal axis so as to access all elements of the SHG susceptibility tensor—which has been described in detail elsewhere [30–32]. Ultrashort (∼100 fs) probe pulses were sourced from a regeneratively amplified Ti:sapphire laser operating at a repetition rate of 5 kHz. A portion of the Ti:sapphire output was directed to an optical parametric amplifier, producing ∼1-eV pump pulses which were delayed relative to the probe pulses with an optical delay line. The incident probe fluence was ∼250 $\mu J\,cm^{-2}$, with the probe spot diameter being ∼100 μm at the sample surface, and the pump pulses (with varying fluence) were focused to a spot roughly ∼400 μm in diameter. Note that all of the SHG intensity is generated instantaneously when the probe interacts with the sample, so any subsequent dynamics induced by the probe pulse itself are not measured by our detector. We verified that the pump-induced static heating at these fluences was insignificant by measuring the temperature dependence of the SHG signal with and without the pump, and noting that the transition temperature is not meaningfully different (see Fig. S23 in Supplemental Material [13]). The (011) plane was found to be the only natural cleavage plane of the sample. The pump was normally incident to the sample surface (to facilitate blocking the reflected pump scatter), and the probe was incident with an angle of ∼10°. The reflected SHG signal was collected with a photomultiplier tube, filtered with a lock-in amplifier operating at the repetition rate of the regenerative amplifier, and correlated with the rotation angle of the grating with an optical rotary encoder and homebuilt oscilloscope. To eliminate potential artifacts due to low-frequency fluctuations in the laser intensity, multiple random sweeps of the delay stage were averaged together for each dataset, and the polarizers were controlled automatically at each delay using custom polarization rotators described in Ref. [55].

C. PTMB measurements

The polarization-dependent optical birefringence (linear dichroism) measurements were conducted using the experimental setup detailed in Ref. [35]. A 633-nm probe laser beam was focused onto a 5-μm spot at surface of the sample, while a 780-nm pump or heating beam was similarly focused onto the same location. To improve the signal-to-noise ratio and eliminate polarization artifacts originating from the experimental setup, the sample temperature was modulated at 2 kHz by passing the pump beam through an optical chopper. The linear dichroism signal was subsequently measured using a standard balanced photodetection scheme

and a lock-in amplifier. Position-dependent measurements of optical birefringence were obtained by scanning the sample position with a piezoelectric scanner. The dependence of the polarization rotation on the probe polarization angle was fit to a sinusoidal function at each spot, and the phase shift parameter extracted from each fit was plotted in Figs. 2(a) and 2(c) (see Supplemental Material, Fig. S22 [13]). Note that the birefringence signal involves contributions from both the lattice and the magnetism, so that the angle extracted from this fit should not be identified with the angle of the AFM order parameter.

D. XRD measurements

XRD data (Supplemental Material, Fig. S8 [13]) were collected at 100 and 180 K on a Bruker-AXS X8 Kappa Duo diffractometer with IμS microsources, coupled to a Photon 3 CPAD detector using Mo Kα radiation ($\lambda = 0.71073$ Å), performing ϕ and ω scans. Reconstructed precession images of the $(0kl)$, $(h0l)$, and $(hk0)$ planes were calculated directly from the diffraction images using algorithms included in the APEX3 [56] software.

ACKNOWLEDGMENTS

The authors thank Clifford Allington, Martin Eckstein, Shiang Fang, Feng Hao, David Hsieh, Honglie Ning, Jia Xu, and Guangua Zhang for several helpful discussions. The authors also acknowledge the MIT SuperCloud and Lincoln Laboratory Supercomputing Center for providing HPC resources that have contributed to the research results reported within this paper. B. T. F., B. L., K. M., Z. S., B. I., T. L., and N. G. acknowledge support from the U.S. Department of Energy, BES DMSE (data taking and analysis), and Gordon and Betty Moore Foundation's EPiQS Initiative Grant No. GBMF9459 (instrumentation). C. L., E. D., A. L.-P., and J. O. acknowledge support from the Quantum Materials program under the Director, Office of Science, Office of Basic Energy Sciences, Materials Sciences and Engineering Division, of the U.S. Department of Energy, Contract No. DE-AC02-05CH11231. G. A. F. gratefully acknowledges support from the NSF through the Center for Dynamics and Control of Materials: an NSF MRSEC under DMR-1720595, NSF DMR2114825, and the Alexander von Humboldt Foundation. R. H. A. d. T., M. A., A. L., and A. A. acknowledge support from the Spanish Ministry of Science and Innovation through Grants No. PID2019–105488 GB-I00, No. TED2021-132074B-C32, and No. PID2022-PID2022-139230NB-I00, the European Commission from the MIRACLE (No. 964450), and the Basque Government through Project No. IT-1569-22. B. L. acknowledges support from the Ministry of Science and Technology of China (2023YFA1407400), the National Natural Science Foundation of China (12374063), and the Shanghai Natural Science Fund for Original Exploration Program (23ZR1479900).

DATA AVAILABILITY

Data supporting the figures within this paper and other findings of this study are available from the contact author upon request.

[1] J. Zhang and R. Averitt, *Dynamics and control in complex transition metal oxides*, Annu. Rev. Mater. Res. **44**, 19 (2014).

[2] D. N. Basov, R. D. Averitt, D. van der Marel, M. Dressel, and K. Haule, *Electrodynamics of correlated electron materials*, Rev. Mod. Phys. **83**, 471 (2011).

[3] E. Dagotto, *Complexity in strongly correlated electronic systems*, Science **309**, 257 (2005).

[4] D. N. Basov, R. D. Averitt, and D. Hsieh, *Towards properties on demand in quantum materials*, Nat. Mater. **16**, 1077 (2017).

[5] A. Kogar, A. Zong, P. E. Dolgirev, X. Shen, J. Straquadine, Y.-Q. Bie, X. Wang, T. Rohwer, I.-C. Tung, Y. Yang *et al.*, *Light-induced charge density wave in* $LaTe_3$, Nat. Phys. **16**, 159 (2020).

[6] M. Mitrano, A. Cantaluppi, D. Nicoletti, S. Kaiser, A. Perucchi, S. Lupi, P. Di Pietro, D. Pontiroli, M. Riccò, S. R. Clark, D. Jaksch, and A. Cavalleri, *Possible light-induced superconductivity in* K_3C_{60} *at high temperature*, Nature (London) **530**, 461 (2016).

[7] D. Fausti, R. I. Tobey, N. Dean, S. Kaiser, A. Dienst, M. C. Hoffmann, S. Pyon, T. Takayama, H. Takagi, and A. Cavalleri, *Light-induced superconductivity in a stripe-ordered cuprate*, Science **331**, 189 (2011).

[8] T. Jungwirth, X. Marti, P. Wadley, and J. Wunderlich, *Antiferromagnetic spintronics*, Nat. Nanotechnol. **11**, 231 (2016).

[9] P. Němec, M. Fiebig, T. Kampfrath, and A. V. Kimel, *Antiferromagnetic opto-spintronics*, Nat. Phys. **14**, 229 (2018).

[10] D. Afanasiev, J. R. Hortensius, B. A. Ivanov, A. Sasani, E. Bousquet, Y. M. Blanter, R. V. Mikhaylovskiy, A. V. Kimel, and A. D. Caviglia, *Ultrafast control of magnetic interactions via light-driven phonons*, Nat. Mater. **20**, 607 (2021).

[11] Z. Sun and A. J. Millis, *Transient trapping into metastable states in systems with competing orders*, Phys. Rev. X **10**, 021028 (2020).

[12] Q. D. Gibson, H. Wu, T. Liang, M. N. Ali, N. P. Ong, Q. Huang, and R. J. Cava, *Magnetic and electronic properties of* $CaMn_2Bi_2$*: A possible hybridization gap semiconductor*, Phys. Rev. B **91**, 085128 (2015).

[13] See Supplemental Material at http://link.aps.org/supplemental/10.1103/PhysRevX.15.011044, which includes Refs. [14–22], for supporting theoretical discussion and additional methodological details.

[14] G. Kresse and J. Furthmüller, *Efficient iterative schemes for ab initio total-energy calculations using a plane-wave basis set*, Phys. Rev. B **54**, 11169 (1996).

[15] G. Kresse and D. Joubert, *From ultrasoft pseudopotentials to the projector augmented-wave method*, Phys. Rev. B **59**, 1758 (1999).

[16] S. L. Dudarev, G. A. Botton, S. Y. Savrasov, C. J. Humphreys, and A. P. Sutton, *Electron-energy-loss spectra and the structural stability of nickel oxide: An* LSDA + U *study*, Phys. Rev. B **57**, 1505 (1998).

[17] P. C. Hohenberg and B. I. Halperin, *Theory of dynamic critical phenomena*, Rev. Mod. Phys. **49**, 435 (1977).

[18] H. T. Stokes, D. M. Hatch, and B. J. Campbell, *Isotropy software suite*, https://iso.byu.edu.

[19] H. J. Zeiger, J. Vidal, T. K. Cheng, E. P. Ippen, G. Dresselhaus, and M. S. Dresselhaus, *Theory for displacive excitation of coherent phonons*, Phys. Rev. B **45**, 768 (1992).

[20] R. R. Birss, *Symmetry and Magnetism* (North-Holland Publishing. Co., Amsterdam, 1964).

[21] *Magnetic Characterization Techniques for Nanomaterials*, edited by C. S. Kumar (Springer, Berlin, 2017).

[22] F. Izumi and K. Momma, *VESTA3 for three-dimensional visualization of crystal, volumetric and morphology data*, J. Appl. Crystallogr. **44**, 1272 (2011).

[23] M. M. Piva, S. M. Thomas, Z. Fisk, J.-X. Zhu, J. D. Thompson, P. G. Pagliuso, and P. F. S. Rosa, *Putative hybridization gap in* $CaMn_2Bi_2$ *under applied pressure*, Phys. Rev. B **100**, 045108 (2019).

[24] C. Lane, M. M. Piva, P. F. S. Rosa, and J.-X. Zhu, *Competition between electronic correlations and hybridization in* $CaMn_2Bi_2$, arXiv:1911.10122.

[25] R. H. Aguilera-del-Toro, M. Arruabarrena, A. Leonardo, M. Rodriguez-Vega, G. A. Fiete, and A. Ayuela, *Magnetic order and strain in hexagonal manganese pnictide* $CaMn_2Bi_2$, arXiv:2410.23053.

[26] I. I. Mazin, $CaMn_2Sb_2$: A fully frustrated classical magnetic system, arXiv:1309.3744.

[27] D. E. McNally, J. W. Simonson, J. J. Kistner-Morris, G. J. Smith, J. E. Hassinger, L. DeBeer-Schmitt, A. I. Kolesnikov, I. A. Zaliznyak, and M. C. Aronson, $CaMn_2Sb_2$*: Spin waves on a frustrated antiferromagnetic honeycomb lattice*, Phys. Rev. B **91**, 180407(R) (2015).

[28] R.-P. Pan, H. D. Wei, and Y. R. Shen, *Optical second-harmonic generation from magnetized surfaces*, Phys. Rev. B **39**, 1229 (1989).

[29] K. L. Seyler, A. de la Torre, Z. Porter, E. Zoghlin, R. Polski, M. Nguyen, S. Nadj-Perge, S. D. Wilson, and D. Hsieh, *Spin-orbit-enhanced magnetic surface second-harmonic generation in* Sr_2IrO_4, Phys. Rev. B **102**, 201113(R) (2020).

[30] B. T. Fichera, A. Kogar, L. Ye, B. Gökce, A. Zong, J. G. Checkelsky, and N. Gedik, *Second harmonic generation as a probe of broken mirror symmetry*, Phys. Rev. B **101**, 241106(R) (2020).

[31] J. W. Harter, L. Niu, A. J. Woss, and D. Hsieh, *High-speed measurement of rotational anisotropy nonlinear optical harmonic generation using position-sensitive detection*, Opt. Lett. **40**, 4671 (2015).

[32] D. H. Torchinsky, H. Chu, T. Qi, G. Cao, and D. Hsieh, *A low temperature nonlinear optical rotational anisotropy spectrometer for the determination of crystallographic and electronic symmetries*, Rev. Sci. Instrum. **85**, 083102 (2014).

[33] S. Reimers, D. Kriegner, O. Gomonay, D. Carbone, F. Krizek, V. Novák, R. P. Campion, F. Maccherozzi, A. Björling, O. J. Amin, L. X. Barton, S. F. Poole, K. A. Omari, J. Michalička, O. Man, J. Sinova, T. Jungwirth, P. Wadley, S. S. Dhesi, and K. W. Edmonds, *Defect-driven antiferromagnetic domain walls in* CuMnAs *films*, Nat. Commun. **13**, 724 (2022).

[34] N. B. Weber, H. Ohldag, H. Gomonaj, and F. U. Hillebrecht, *Magnetostrictive domain walls in antiferromagnetic* NiO, Phys. Rev. Lett. **91**, 237205 (2003).

[35] A. Little, C. Lee, C. John, S. Doyle, E. Maniv, N. L. Nair, W. Chen, D. Rees, J. W. F. Venderbos, R. M. Fernandes, J. G. Analytis, and J. Orenstein, *Three-state nematicity in the triangular lattice antiferromagnet* $Fe_{1/3}NbS_2$, Nat. Mater. **19**, 1062 (2020).

[36] C. Lee, P. Vir, K. Manna, C. Shekhar, J. E. Moore, M. A. Kastner, C. Felser, and J. Orenstein, *Observation of a phase transition within the domain walls of ferromagnetic* $Co_3Sn_2S_2$, Nat. Commun. **13**, 3000 (2022).

[37] M. Fiebig, V. V. Pavlov, and R. V. Pisarev, *Second-harmonic generation as a tool for studying electronic and magnetic structures of crystals: review*, J. Opt. Soc. Am. B **22**, 96 (2005).

[38] M. Fiebig, D. Fröhlich, B. B. Krichevtsov, and R. V. Pisarev, *Second harmonic generation and magnetic-dipole-electric-dipole interference in antiferromagnetic* Cr_2O_3, Phys. Rev. Lett. **73**, 2127 (1994).

[39] M. Fiebig, D. Fröhlich, T. Lottermoser, V. V. Pavlov, R. V. Pisarev, and H.-J. Weber, *Second harmonic generation in the centrosymmetric antiferromagnet* NiO, Phys. Rev. Lett. **87**, 137202 (2001).

[40] M. Fiebig, D. Fröhlich, G. Sluyterman v. L, and R. V. Pisarev, *Domain topography of antiferromagnetic* Cr_2O_3 *by second-harmonic generation*, Appl. Phys. Lett. **66**, 2906 (1995).

[41] Note that, in general, we do not expect the direction of the Néel vector to be qualitatively apparent from the RASHG pattern, since the (001) easy plane of the AFM order is not the plane which is normal to the optical axis [which is (011), the natural cleavage plane of $CaMn_2Bi_2$, in our measurement geometry; see Fig. 1].

[42] R. Boyd, *Nonlinear Optics*, 3rd ed. (Academic Press, New York, 2008).

[43] T. Higo, K. Kondou, T. Nomoto, M. Shiga, S. Sakamoto, X. Chen, D. Nishio-Hamane, R. Arita, Y. Otani, S. Miwa, and S. Nakatsuji, *Perpendicular full switching of chiral antiferromagnetic order by current*, Nature (London) **607**, 474 (2022).

[44] Z. Ni, A. V. Haglund, H. Wang, B. Xu, C. Bernhard, D. G. Mandrus, X. Qian, E. J. Mele, C. L. Kane, and L. Wu, *Imaging the Néel vector switching in the monolayer antiferromagnet* $MnPSe_3$ *with strain-controlled Ising order*, Nat. Nanotechnol. **16**, 782 (2021).

[45] J. Zhu, Q. Li, J. X. Li, Z. Ding, C. Y. Hua, M. J. Huang, H.-J. Lin, Z. Hu, C. Won, and Y. Z. Wu, *Strain-modulated antiferromagnetic spin orientation and exchange coupling in* Fe/CoO(001), J. Appl. Phys. **115**, 193903 (2014).

[46] A. Koziol-Rachwal, M. Slezak, M. Zajac, P. Drozdz, W. Janus, M. Szpytma, H. Nayyef, and T. Slezak, *Control of spin orientation in antiferromagnetic* NiO *by epitaxial strain and spin–flop coupling*, APL Mater. **8**, 061107 (2020).

[47] P. E. Dolgirev, M. H. Michael, A. Zong, N. Gedik, and E. Demler, *Self-similar dynamics of order parameter*

fluctuations in pump-probe experiments, Phys. Rev. B **101**, 174306 (2020).

[48] K. A. Cremin, J. Zhang, C. C. Homes, G. D. Gu, Z. Sun, M. M. Fogler, A. J. Millis, D. N. Basov, and R. D. Averitt, *Photoenhanced metastable c-axis electrodynamics in stripe-ordered cuprate* $La_{1.885}Ba_{0.115}CuO_4$, Proc. Natl. Acad. Sci. U.S.A. **116**, 19875 (2019).

[49] C. L. Smallwood, J. P. Hinton, C. Jozwiak, W. Zhang, J. D. Koralek, H. Eisaki, D.-H. Lee, J. Orenstein, and A. Lanzara, *Tracking Cooper pairs in a cuprate superconductor by ultrafast angle-resolved photoemission*, Science **336**, 1137 (2012).

[50] S. Parkin and S.-H. Yang, *Memory on the racetrack*, Nat. Nanotechnol. **10**, 195 (2015).

[51] M. G. Kim, A. Barbour, W. Hu, S. B. Wilkins, I. K. Robinson, M. P. M. Dean, J. Yang, C. Won, S.-W. Cheong, C. Mazzoli, and V. Kiryukhin, *Real-space observation of fluctuating antiferromagnetic domains*, Sci. Adv. **8**, eabj9493 (2022).

[52] H. Watanabe and Y. Yanase, *Group-theoretical classification of multipole order: Emergent responses and candidate materials*, Phys. Rev. B **98**, 245129 (2018).

[53] H. Watanabe and Y. Yanase, *Nonlinear electric transport in odd-parity magnetic multipole systems: Application to* Mn*-based compounds*, Phys. Rev. Res. **2**, 043081 (2020).

[54] H. Watanabe and Y. Yanase, *Symmetry analysis of current-induced switching of antiferromagnets*, Phys. Rev. B **98**, 220412(R) (2018).

[55] K. Morey, B. T. Fichera, B. Lv, and N. Gedik (to be published).

[56] Bruker, APEX3, Bruker-AXS Inc., Madison, Wisconsin, 2022.